Opto-Electronic Engineering

Article

2017, Vol 44, Issue 3

Two dimensional subdiffraction focusing beyond the near-field diffraction limit via metasurface

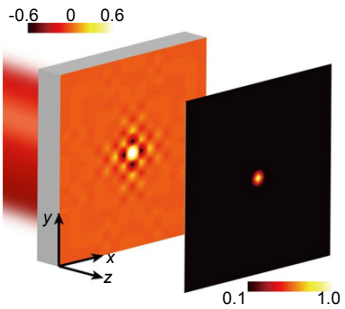

Maowen Song and Honglin Yu*

Key Laboratory of Optoelectronic Technology and System, Ministry of Education, Chongqing University, Chongqing 400044, China

Abstract: Near-field plates with the capabilities of modulating the near-field pattern and forcing the incident wave to a subwavelength spot have been experimentally investigated at microwave wavelengths. Their superlensing properties result from the radiationless electromagnetic interference. However, the material's loss and limitations of state-of-the-art nanofabricating technology pose great challenges to scale down the microwave near-field plates to the infrared or optical region. In this paper, a related but alternative approach based on metasurface is introduced which breaks the near-field diffraction limit at mid-infrared region (10.6 μm). The metasurface consists of periodic arrangement of chromium dipolar antennas with the same geometry but spatially varying orientations, which plays the dual roles in achieving the prescribed amplitude modulation and the abrupt π phase change between the subwavelength neighboring elements. As a result, a two dimensional subdiffraction focus as small as $0.037\lambda^2$ at ~0.15λ above the metasurface is presented. In addition, the broadband response and ease fabrication bridge the gap between the theoretical investigation and valuable applications, such as near-field data storage, subdiffraction imaging and nanolithography.

Keywords: metasurface; radiationless electromagnetic interference; near-field focusing; subdiffraction

DOI: 10.3969/j.issn.1003-501X.2017.03.008 **Citation:** *Opto-Elec Eng*, 2017, **44**(3): 331−339

1 Introduction

The past decade has witnessed large numbers of optical systems designed for focusing electromagnetic radiation to spots of subwavelength dimension [1-10]. Unlike the diffraction limited plates or lenses, the participant of the evanescent field is necessary for near-field subwavelength focusing. Motivated by the fascinating applications such as detecting the object's near-field details, achieving distinct nanolithography and noncontact sensing, sharp tips [1-3], constraining the incident field to extremely small spot, successfully realized subdiffraction focusing by capturing the evanescent waves before they vanish. However, deep subwavelength spot is generated at the price of extremely short working distance, which increases the complexity of near-field measurement and roadblocks their transition to practical applications. It is taken for granted that it is more difficult to obtain a smaller spot size for a longer working distance (focal length) due to the exponential decay of the evanescent waves [8]. In order to challenge such near-field diffraction limit by producing a subdiffraction focus at a larger distance, near-field plate (NFP) which is capable of setting up a rapidly oscillatory field that converges at the prescribed position was proposed by Merlin in 2007 [11]. The concept of perfect focusing results from radiationless electromagnetic interference (REI), a process that forces the incident wave to a predicted spot and removes the background fields. The NFP was then experimentally realized by alternating inductive and capacitive components to modulate the prescribed surface impedances. Interestingly, the patterned surface focuses the source field oscillating at 1 GHz to a deep subwavelength line with a full width at half maximum (FWHM) of ~0.055 GHz [12]. However, most NFPs are designed and realized at microwave frequency [11-15]. It seems impossible to scale down those samples directly to the size corresponding to infrared or optical region since metallic loss and plasmonic response come into function, let alone abrupt modulations of amplitude and phase are required in the proximity of the structure.

Metamaterials [16-21], with the robust and flexible architectures to engineer the light-matter interactions successfully usher the occurrence of the optical NFP by the

Received 17 November 2016; accepted 10 January 2017
* E-mail: hlyu@cqu.edu.cn

metal-insulator-metal (MIM) waveguide arrays [22-23]. The variable refractive indexes and widths of each insulator channel provide some degrees of freedom to modulate the oscillatory field to form a predicted focus. However, high aspect ratio insulator layers sandwiched by the lossy metal walls pose great challenges to fabricate the architecture. In recent years, a monolayer of plasmonic antennas which is also called "metasurface" serves as an effective method to manipulate wavefront of incident wave [24-33]. In this case, the material loss is not a major problem and the fabricating process can be simplified since alignment between different layers is not required. Although metasurface is a new member in the big family of nanophotonics, it has shown huge potentials in novel optics devices, especially ultrathin metalens proposed recently [34-38]. However, all the metasurface based flat lenses work on travelling waves so that the focuses are diffraction limited or surrounded by obvious background fields [38].

In this paper, we design an ultrathin (~0.007λ) metasurface based NFP to achieve two dimensional subdiffraction focus exceeding the near-field diffraction limit which has not been reported to date. The physics inside resembles the Fresnel plate but the difference is that the subdiffraction focusing properties of such evanescent-field lens stem from the interference of radiationless electromagnetic waves. According to the back-propagation theory [11], a rapidly oscillatory electromagnetic field (simultaneously modulated amplitude and phase between subwavelength neighboring elements) in the proximity of NFP is necessary to force the incident wave to a subwavlength spot. The metasurface proposed here consists of periodic arrangement of chromium dipolar antennas with the same geometry but spatially varying orientations. When a linearly polarized (LP) light illuminates the structure, partially scattered wave converts into the cross polarized light. The modulated amplitude is determined by the orientations of the dipolar antennas and the tuned phase is binary (0 and π), depending on the angle between the incident polarization and spatial orientations of the dipolar antennas. As a result, a deep subwavelength spot as small as 0.037λ^2 at ~0.15λ above the metasurface has been numerically demonstrated when the incident wavelength is 10.6 μm. Theoretically, the focus spot can be arbitrarily small at the price of diminished lattice constant (pixel) and low efficiency.

2 Principles and results

2.1 Back propagation theory

It should be remembered that the design of NFP relies on the back-propagated calculation theory with four basic steps [11-14]. According to this inverse construction, the desired field distribution at focal plane should be first defined. For the implementation of two dimensional subdiffraction focus, we assume that the focus spot exhibits the profile with the following functional form:

$$E_l = \frac{\mathrm{e}^{-k_{\max} l} k_{\max} l \sin(\pi k_{\max} \sqrt{x^2 + y^2})}{\pi k_{\max} \sqrt{x^2 + y^2}}, \quad (1)$$

where $k_{\max}$ is a constant determining the spot size and l represents the working distance (focal length). After solving a Fourier transformation to the field at the focal plane, we back propagate the plane wave spectrum with a transfer function as follow:

$$H = \exp(-\mathrm{i} k_z l), \quad (2)$$

$$k_z = \mathrm{i}\sqrt{k_x^2 + k_y^2 - k_0^2}. \quad (3)$$

This choice of the wavevector k_z is determined by the requirements that the evanescent waves transmit and decay in the positive z direction. k_0 is the incident wavevector described as $2\pi/\lambda_0$. By summing the calculated plane wave spectrum in the proximity of the surface, the exiting field E_0 of the NFP has been recovered as follow:

$$E_0 = \frac{1}{4\pi^2} \iint \int_{-\infty}^{+\infty} \int \frac{\mathrm{e}^{-k_{\max} l} k_{\max} l \sin(\pi k_{\max} \sqrt{x^2 + y^2})}{\pi k_{\max} \sqrt{x^2 + y^2}} \times \exp(-\mathrm{i} k_z l) \mathrm{d}x \mathrm{d}y \mathrm{d}k_x \mathrm{d}k_y. \quad (4)$$

The metasurface based NFP should be designed to generate the field profile indicated by Eq. (4) at the exiting surface. Specifically, the NFP is normally illuminated by the x-polarized plane wave at a wavelength of 10.6 μm. The $k_{\max}$ is predicted to be 2.12k_0 and the focal plane is assumed at 1.5 μm above the NFP. This value is much longer than 0.45 μm for the near-field diffraction limit, which can be considered that the field emanating from the exiting surface fades to 1/e of its original value with a characteristic length l_c [9-10]:

$$l_c = \frac{1}{4\pi} \cdot \frac{1}{\sqrt{\delta^{-2} - \varepsilon \lambda_0^{-2}}}, \quad (5)$$

where ε and λ_0 are the permittivities of air and the wavelength of incident light in vacuum, respectively. In Ref. [9], δ indicates the lattice constant of the line-array sample, corresponding to a characteristic wavevector k_g. In the case of subdiffraction focusing, the spot size is determined by the highest-order of wavevector contributing to the focus. δ in this formula can be assumed as $2\pi/k_{\max}$, which has been explained in our previous work[10].

Fig. 1 schematically shows that the NFP tailors the incident field to the patterned distribution (Eq. (4)) which is required to generate a two dimensional subdiffraction focus (Eq. (1)). Abruptly modulated amplitude and π phase inverse between neighboring elements at the exiting surface seem inevitable since they play dual roles in forcing the wave to subwavelength spot and remove the background fields. At microwave region, the amplitude and phase can be accurately manipulated when the transmitted energy is low [13]. The inductive sheets and capacitive sheets induce a phase of +90° and -90°, respec-

tively. As a result, alternating inductive and capacitive impendence sheets can produce π phase inverse. The varying amplitude of the transmitted field can be controlled by the magnitude of the sheet reactance [11-13]. However, it is not effective to directly scale down the capacitors and inductors to realize the oscillatory field profile due to the change of the material's properties at infrared and visible regions. Fortunately, metasurfaces provide us a platform to solve this problem.

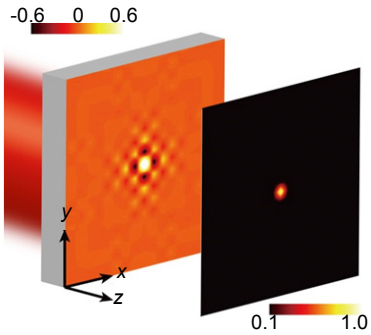

Fig. 1 Schematic shows the phase and the amplitude distributions in the proximity of the NFP which is required to generate the predicted focus via REI. The red region indicates the normally incident wave. The NFP locates at z=0 and the focal plane locates at z=l.

2.2 Metasurface design

The ideal metasurface based NFP model in this case is homogeneously divided into n×n square segments. n is the number of segments along the horizontal or vertical direction and each one spreads 2.5 μm×2.5 μm, which is related to the prescribed k_{max}. Lots of building blocks assure the sufficient reproduction of the back-propagated field at the exiting surface of NFP, but the required electric field amplitude gradually diminishes at the outer positions. When the number of segments is 15×15, the transmitted field at outer locations has decreased by several orders than the magnitude in center. So the outermost fields make no contributions to the focus. The calculated values of amplitude and phase for each segment are depicted in Fig. S1 (seeing supplementary information). In the design, we approximate these phases by labeling them to binary values (0 or π) according to the principle of proximity. Calculated results demonstrate that this simplification has no influence on the focus quality as shown in Fig. S2. For the design of the NFP, two goals are very important: 1) the amplitude modulation can vary smoothly from zero to the maximum; 2) binary phase inverse can be achieved within a small fraction of the wavelength. Interestingly, periodic arrangement of dipolar antennas is the natural candidate to implement the predicted NFP for LP excitation.

Fig. 2(a) shows a schematic of the designed metasurface that consists of chromium dipolar antennas, which are arranged in two dimensional arrays with a lattice constant of 2.5 μm in both x and y directions. The length and width of the antennas with ultrathin thickness of h = 75 nm are d = 1.8 μm and w = 0.6 μm, respectively. The permittivity of chromium is obtained from the Ref. [39] and the refractive index of silicon substrate is considered as 3.4 when a LP plane wave at the wavelength of 10.6 μm normally illuminate the sample from the substrate side. In order to investigate the physics inside, the finite element method (FEM) based on the commercial software packages solver CST 2016 is adopted to analyze the building block where unit cell boundary conditions are used along the transverse directions. The unit cell is meshed with little tri-angle elements and local mesh refinement has been ensured ultrafine especially around the edges and corners of the dipolar antenna. Fig. 2(b) depicts the calculated amplitude and phase variation versus different orientations θ of each antenna. Obviously, the scattered amplitude of the transmitted field with the cross polarization is continuously manipulated by parameter θ, while the phase remains almost flat except for the abrupt π inverse at θ= 90°. It can be concluded that θ

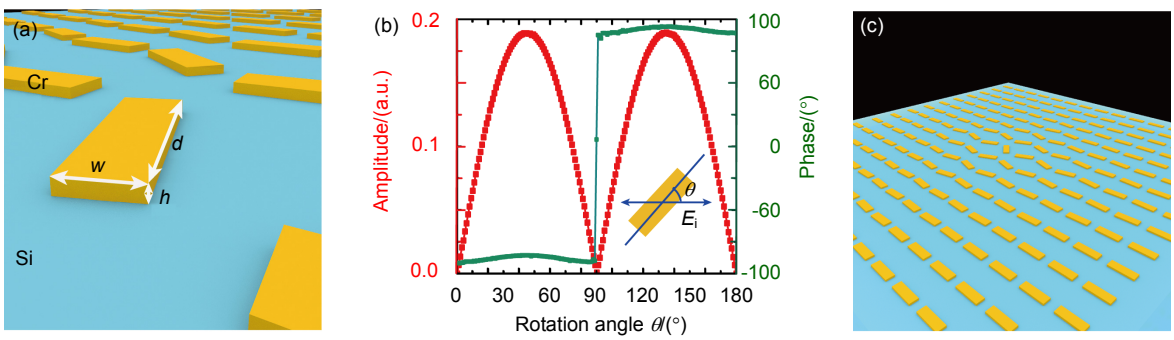

Fig. 2 (a) Schematic of chromium dipolar antennas with length d, width w, and thickness h. All the antennas reside at the surface of silicon substrate. (b) Calculated transmitted amplitude (red square curve) and phase (green solid curve) of periodically arrayed building blocks versus the rotation angle θ between the orientation of antenna and the incident polarization E_i. Obviously, smooth amplitude variation has been achieved and a π phase jump occurs when the rotation angle exceeds 90°. (c) Schematic of the metasurface based NFP, which consists of periodic arrangement of chromium dipolar antennas with the same geometry but spatially varying orientations.

plays the dual roles in manipulating the amplitude of partially scattered field with cross polarization and realizing the prescribed binary phase inverse. The transmitted *y*-polarized electric field can be written as follows:

$$E_y = \frac{\theta - 90}{|\theta - 90|} \cdot 0.189 \cdot E_x \sin(2\theta). \quad (6)$$

where E_x denotes the amplitude of the *x*-polarized incident plane wave, the sign of E_y represents the transmitted phase and θ ranges from 0° to 180°. Thus, this functional form provides a facile and effective method to design a metasurface with simultaneous binary phase control and smoothly modulated amplitude profile, facilitating the two goals proposed before to design a NFP. Fig. 2(c) shows a perspective view of our metasurface based NFP, specific orientation of each dipolar antenna is determined by data in Fig. S1 and Eq. (6).

2.3 Focusing quality

Fig. 3(a) depicts simulated results of the *y*-polarized electric field intensity distribution at focal plane l = 1.5 μm. A distinct two dimensional focusing spot is presented and the field intensity is normalized to the maximum value. We show in Figs. 3(b) and 3(c) the cross-sectional plots of the transmitted *y*-polarized electric field at *x*-*z* plane (*y*=0) and *y*-*z* plane (*x*=0), respectively. The electric field alternates its sign between adjacent neighbors, which means that a π phase inverse occurs to squeeze the central lobe and remove the *y*-polarized background fields. Such a behavior of beam coupling is the process of REI. The focal plane is determined by where the central lobe spread since the magnitude of the side lobes decreases to a certain amount (the white dashed lines). The focus qualities have been further investigated by the field profiles plotted along the horizontal and vertical lines passing the spot center in Fig. 3(a). The results are depicted in Figs. 3(d) and 3(e) for the cases of horizontal direction and vertical direction, respectively. It can be seen that a distinct focus generates with field profile (red solid curves) in a nearly perfect agreement to the expected one (blue circle curves), exceeding the near-field diffraction limit (green dashed curves) at 1.5 μm above the NFP.

However, the relatively larger intensity of the side lobes leads to occurrence of the *y*-polarized background fields and influences the shape of the spot compared with the predicted one. The less-than-perfect two dimensional subdiffraction focusing results from the imperfect reproduction of the exiting field in the proximity of the metasurface as prescribed by Eq. (4). Several drawbacks restrict the performance of the metasurface based NFP, such as high-order modes confined at the corners and edges of the dipolar antennas and the unexpected coupling between the neighboring elements. In order to investigate the influence caused by the high-order modes, the amplitudes of the *y*-polarized electric field along the horizontal direction passing the center (white dashed line) at different planes have been plotted as shown in Fig. 4. The main lobe of the black square curve has two ultra sharp peaks located at where the edges of the central antenna reside (indicated by the purple arrows). This phenomenon is induced by the high-order electromagnetic

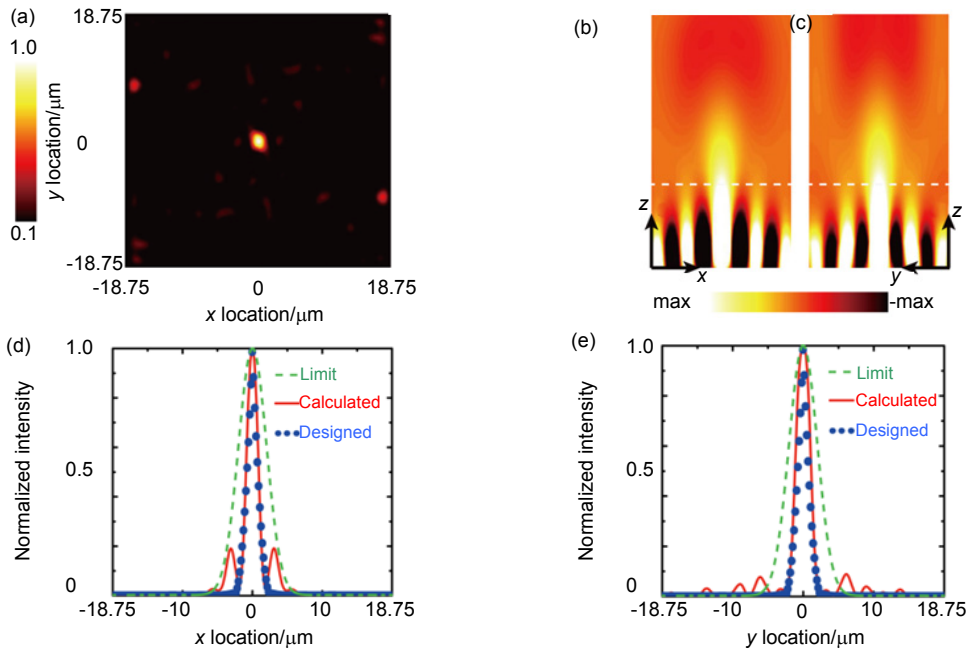

Fig. 3 (a) Schematic of *y*-polarized electric field intensity ($|E_y|^2$) distribution at focal plane. A two dimensional focus spot can be clearly seen as expected. (b) and (c) describe the cross-sectional plots of the transmitted *y*-polarized field ($|E_y|$) in the *x*-*z* plane, *y*-*z* plane, respectively, which show the process of radiationless electromagnetic interference. Alternative sign of the electric field indicates a π phase jump between the neighboring elements. The white dashed lines indicate the position of the focal plane. (d) and (e) show the calculated field profile (red solid curves) agrees well with the designed ones (blue circles), exceeding the near-field diffraction limit (green dashed curves). The discrepancies are originated from the relatively larger magnitude of the side lobes than the expected values.

mode confined at metallic edges and corners, which have also been discussed in Ref. [10] and Ref. [22]. When the field transmits to the plane at z=0.1 μm, sharply peaked components still dominate the profile but the magnitude decreases a lot especially at the positions corresponding to the metallic edges and corners. Blue triangle curve depicts that the sharply peaked fields decay rapidly toward to the focal plane, whose maximum amplitude is only about a quarter of that at the exiting surface (z=0 μm). Sharply peaked components almost vanish when the field transmits to the plane at z=0.5 μm as indicated by the purple triangle curve. When z reaches 1 μm, there are no sharp peaks in the field profile, which solely results from the process of radiationless electromagnetic interference (REI) and finally leads to a subwavelength focus at the predicted focal plane z=1.5 μm. All the values have been normalized to the incident magnitude. It can be considered that the high-order modes excited and confined at the corners and edges of the dipolar antennas have a little influence on the performance of the NFP. Thus, the coupling between the neighboring elements seems to be the main cause of imperfect reproduction of the exiting field at the surface of NFP. The results in Fig. 2(b) are obtained in the case of the building block with ideally periodic boundary condition. However, each dipolar antenna resided in the NFP varies relatively different orientations to its neighbors. In addition, the center to center distance of the adjacent antennas is in deep subwavelength size. Both the reasons result in the occurrence of unexpected coupling between the neighboring elements, which slightly perturb the field distribution compared with the predicted values.

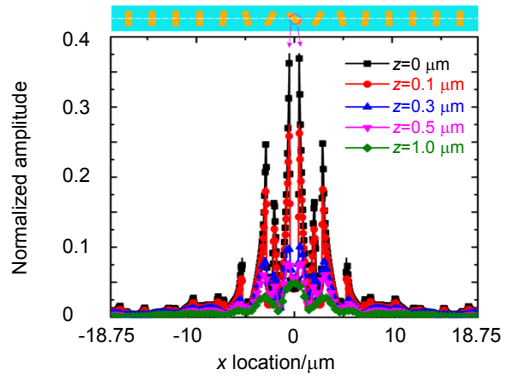

Fig. 4 The *y*-polarized fields profiles along the horizontal direction as indicated by white dashed line at different planes. The inset depicts the periodic arrangement of chromium dipolar antennas at the central array. The purple arrows indicate where the sharply peaked fields locate.

3 Discussion

Our work is reminiscent of, but the physics inside is quite different from the optical NFPs proposed before [4,10,22-23]. One implantation of the REI focusing relied on structural metal film, which excites an asymmetric surface plasmon modes to generate the oscillatory field profile for subdiffraction focusing [4]. The amplitude modulation is achieved by variant thickness of the structural metal and the π phase inverse is realized at the adjacent edges of the metallic walls. However, this structural metal film based NFP generates an one dimensional focus (linear focus) since the structure only offers the platform for amplitude modulation by transverse magnetic polarized Fresnel formula. In addition, accurate control of the continuously various thicknesses of the metal film is difficult to be experimentally demonstrated. The metasurface based NFP relaxes such problems since the modulations of amplitude and phase are both dependent on the rotation angle of the dipolar antenna. Periodic arrangement of ultrathin chromium resonators can be easily compatible with electron beam lithography (EBL). The variable MIM waveguide arrays are also capable of modulating the amplitude and phase of the exiting field for subwavelength focusing at visible regime. This architecture based NFP relies on the highest order guided modes [22] or Fano resonance [23] excited by high aspect ratio waveguide, which poses a bottleneck challenged by the state-of-the-art fabricating technology. Fortunately, a single layer of the chromium dipolar antennas can function as a NFP by direct LP plane wave illumination. Different from the coupling between the propagating modes in the thick MIM waveguide, the partially scattered waves in the proximity of the metasurface converge to the predicted focus resulting from a static form of interference. Our previous work [10] proposed a ring-disk complementary architecture to achieve REI focus. Benefitting from the plasmonic Fano resonance originated from interference between hybrid plasmon resonance and the continuum of propagating waves through the silver film, a deep subwavelength spot ($0.0045\lambda^2$) generates at 36 nm above the surface where goes beyond the near-field diffraction limit. However, the imperfect reproduction of the field caused by the simple structure inevitably results in the less ideal focusing spot. Metasurface based NFP benefits from more degrees of freedom in simultaneously controlling the dimensions, geometry and orientation of the antennas to optimize the reproduction and enhance the efficiency.

The first step to design a NFP involves determining the operating frequency, predicting the functional form of the focus and finding the field required to produce the spot. Thus almost all the NFPs were only available at one incident wavelength since the resolution, focal length and dimensions of the building blocks are all related to the source frequency, especially those NFPs equipped with intricate elements [11-15] or function based on spectrally narrow Fano resonance [10,23]. Our metasurface based NFP has been designed at a wavelength of 10.6 μm. Interestingly, we further explore the same metasurface and numerically find its REI focusing property can be extended to broadband wavelengths ranging from 10 μm to 13 μm.

Figs. 5(a)~5(c) depict the *y*-polarized electric field intensity distribution at focal plane I = 1.5 μm with incident wavelength of 10 μm, 12 μm and 13 μm, respectively. It can be seen that the NFP exhibits ideal broadband response for two dimensional subwavelength focusing. In addition, the most fascinating characteristic of this device is that the broadband focusing quality remains high at the same focal plane, differing from the broadband plasmonic gradient metalens proposed before [37,40] whose focal length decreases rapidly for longer incident wavelength. Figs. 5(d)~5(f) (Figs. 5(g)~5(i)) depict the field profiles plotted along horizontal (vertical) lines passing the spot center in Figs. 5(a)~5(c), respectively.

Our design of the metasurface based NFP combines a number of important advantages: precise amplitude and phase control, ease fabrication, broadband subdiffraction focusing at the same focal plane and two dimensional spot exceeding the near-field diffraction limit. All the structural parameters in this investigation rely on the feasible fabricating technology. The focus spot can be much smaller by diminishing the lattice constant and the NFP can be more efficient by increasing the thickness of the chromium antennas or exploring other plasmonic materials. Periodic arrangement of chromium dipolar antennas in vicinity of a reflecting layer can enhance the maximum *y* polarized electric field amplitude to 80% of the incident magnitude as shown in Fig. S4. Scanning near-field optical microscope (SNOM)[41] offers the platform to measure the polarized focus in the near-field region. With increasing demands of novel applications and the progress of the nanofabrication technology, metasurface based optical NFP will be experimentally demonstrated, which has not been reported to date. We believe the periodic arrangement of dipolar antennas will be a very effective tool to achieve two dimensional subdiffraction focus at broadband wavelengths.

4 Conclusion

In this work, we theoretically achieved a broadband NFP based on metasurface, which consists of periodic arrangement of chromium dipolar antennas with variant orientations. The focus quality is determined by how precise the exiting field at the surface of NFP can be implemented. Fortunately, the rotation angle of the antenna simultaneously controls the amplitude of partially scattered cross polarization field and the prescribed binary phase distribution when LP wave feeds the NFP. As a result, a deep subwavelength spot as small as $0.037\lambda^2$ generates at 1.5 μm above the metasurface which is in nearly

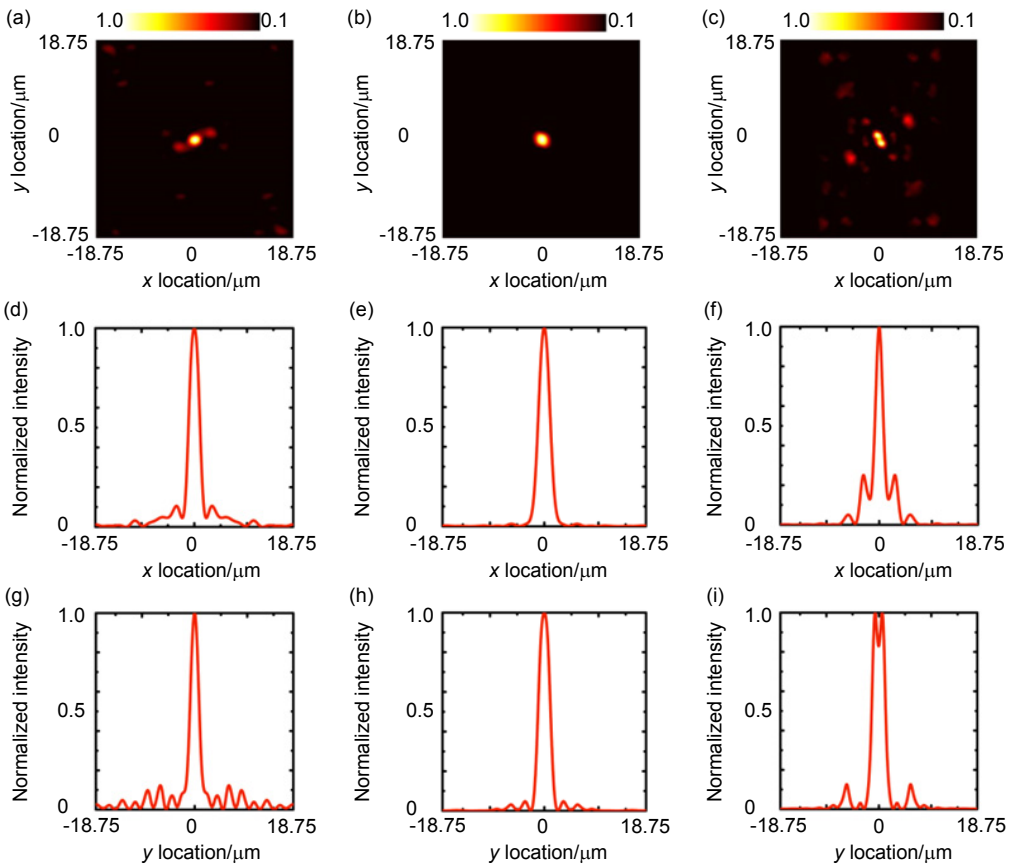

Fig. 5 (a)~(c) *y*-polarized electric field intensity ($|E_y|^2$) distribution at focal plane at the incident wavelength of 10 μm, 12 μm and 13 μm, respectively. The red curves indicate the normalized field intensity profile plotted along (d)~(f) *x* and (g)~(i) *y* direction.

perfect agreement to the predicted one. Different from those metasurface based lens proposed before, this evanescent-field lens achieve broadband subdiffraction focusing at the same focal plane. In addition, easily compatible with the popular fabricating technology and scaled to be functional at near infrared and optical regions bridge the gap between the theory of REI and valuable applications, such as near-field data storage, subdiffraction imaging and nanolithography.

5 Supplementary information

5.1 The amplitude and phase distribution at the exiting surface of NFP

When the three dimensional subdiffraction focusing is predicted to exhibit the profile as indicated by Eq. (1), we amplify the evanescent wave and back propagate the plane wave spectrum after solving a Fourier transformation to the field at the focal plane. Fig. S1 shows the amplitude (red numbers) and phase (green numbers) distribution for each segment which is required to achieve the predicted focus. The building block responsible for the max modulated amplitude locates at the center, where the value is assumed to be 10. All the other values have been normalized to the maximum.

For simplification, we approximate these phases by labeling them to binary values (0 or π) according to the principle of proximity. It amounts to that the values located at -90° to 90°. can be estimated as 0°, and the others are labeled by π. Fig. S2 shows the comparison between

0.033 171.7	0.01 -180	0.01 -151.6	0.011 -152.1	0.125 -178.9	0.155 0.168	0.085 179.1	0.037 178.1	0.085 179.1	0.155 0.168	0.125 -178.9	0.011 -152.1	0.01 -151.6	0.01 -180	0.003 171.7
0.01 -180	0.046 0.015	0.064 0.638	0.052 2.459	0.198 0.994	0.228 179.2	0.17 0.71	0.017 4.964	0.17 0.71	0.228 179.2	0.198 0.994	0.052 2.459	0.064 0.638	0.046 0.015	0.01 -180
0.01 -151.6	0.064 0.638	0.068 174.5	0.061 172.6	0.193 178.7	0.166 -0.133	0.115 -178.3	0.044 -5.853	0.115 -178.3	0.166 -0.133	0.193 178.7	0.061 172.6	0.068 174.5	0.064 0.638	0.01 -151.6
0.011 -152.1	0.052 2.459	0.061 172.6	0.004 95.95	0.085 -3.22	0.092 -173	0.13 -174.9	0.057 -10.6	0.13 -174.9	0.092 -173	0.085 -3.22	0.004 95.95	0.061 172.6	0.052 2.459	0.011 -152.1
0.125 -178.9	0.198 0.994	0.193 178.7	0.085 -3.22	0.072 -11.81	0.043 -17.79	0.486 -0.188	0.514 179.4	0.486 -0.188	0.043 -17.79	0.072 -11.81	0.085 -3.22	0.193 178.7	0.198 0.994	0.125 -178.9
0.155 0.168	0.228 179.2	0.166 -0.133	0.092 -173	0.043 -17.79	0.023 17.71	0.787 177.2	1.55 2.025	0.787 177.2	0.023 17.71	0.043 -17.79	0.092 -173	0.166 -0.133	0.228 179.2	0.155 0.168
0.085 179.1	0.17 0.71	0.115 -178.3	0.13 -174.9	0.486 -0.188	0.787 177.2	1.499 3.5	4.046 178.4	1.499 3.5	0.787 177.2	0.486 -0.188	0.13 -174.9	0.115 -178.3	0.17 0.71	0.085 179.1
0.037 178.1	0.017 4.964	0.044 -5.853	0.057 -10.6	0.514 179.4	1.55 2.025	4.046 178.4	10 0.823	4.046 178.4	1.55 2.025	0.514 179.4	0.057 -10.6	0.044 -5.853	0.017 4.964	0.037 178.1
0.085 179.1	0.17 0.71	0.115 -178.3	0.13 -174.9	0.486 -0.188	0.787 177.2	1.499 3.5	4.046 178.4	1.499 3.5	0.787 177.2	0.486 -0.188	0.13 -174.9	0.115 -178.3	0.17 0.71	0.085 179.1
0.155 0.168	0.228 179.2	0.166 -0.133	0.092 -173	0.043 -17.79	0.023 17.71	0.787 177.2	1.55 2.025	0.787 177.2	0.023 17.71	0.043 -17.79	0.092 -173	0.166 -0.133	0.228 179.2	0.155 0.168
0.125 -178.9	0.198 0.994	0.193 178.7	0.085 -3.22	0.072 -11.81	0.043 -17.79	0.486 -0.188	0.514 179.4	0.486 -0.188	0.043 -17.79	0.072 -11.81	0.085 -3.22	0.193 178.7	0.198 0.994	0.125 -178.9
0.011 -152.1	0.052 2.459	0.061 172.6	0.004 95.95	0.085 -3.22	0.092 -173	0.13 -174.9	0.057 -10.6	0.13 -174.9	0.092 -173	0.085 -3.22	0.004 95.95	0.061 172.6	0.052 2.459	0.011 -152.1
0.01 -151.6	0.064 0.638	0.068 174.5	0.061 172.6	0.193 178.7	0.166 -0.133	0.115 -178.3	0.044 -5.853	0.115 -178.3	0.166 -0.133	0.193 178.7	0.061 172.6	0.068 174.5	0.064 0.638	0.01 -151.6
0.01 -180	0.046 0.015	0.064 0.638	0.052 2.459	0.198 0.994	0.228 179.2	0.17 0.71	0.017 4.964	0.17 0.71	0.228 179.2	0.198 0.994	0.052 2.459	0.064 0.638	0.046 0.015	0.01 -180
0.003 171.7	0.01 -180	0.01 -151.6	0.011 -152.1	0.125 -178.9	0.155 0.168	0.085 179.1	0.037 178.1	0.085 179.1	0.155 0.168	0.125 -178.9	0.011 -152.1	0.01 -151.6	0.01 -180	0.003 171.7

Fig. S1 Numerically obtained amplitude (red numbers) and phase (green numbers) values for each segment.

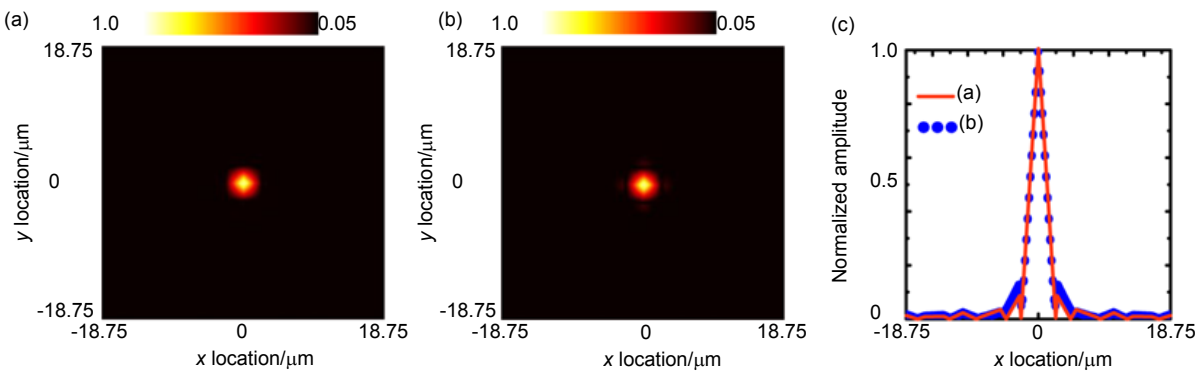

Fig. S2 (a),(b) The numerically obtained *y* polarized field amplitude (E_y) distribution at the focal plane with the original parameters in Fig. S1 and the simplified binary phase. (c) The field profiles plotted along the horizontal line passing the spot center in (a) (red solid curve) and (b) (blue dot curve).

the focus quality calculated by the phase values in Fig. S1 and the binary estimation. Interestingly, the red solid curve (original values) overlaps the blue dot curve (simplified values). It can be concluded that this simplification has no influence on the focus quality.

This NFP can be also realized by equipping the metasurface with C or V shaped plasmonic antennas [1] if we use the originally calculated phase distribution (green numbers) in Fig. S1. However, the optimization process would be much more intricate and the fabrication tolerances would be less since various combinations of amplitude and phase modulation correspond to lots of different geometric antennas.

5.2 The reflective mode

In order to enhance the efficiency of REI focusing, periodic arrangement of chromium dipolar antennas are separated from a reflective plane by a silicon spacer. Fig. S3 shows the schematic of the reflective mode NFP. The substrate is gold and the incident wave illuminates the structure from the surface. All the structural parameters are the same as the transmitted mode except for the thickness of silicon h_d, which has been optimized to 2.2 μm.

Fig. S4(a) depicts the reflected amplitude of the partially scattered wave with cross polarization versus different orientations θ. The maximum modulated y polarized electric field amplitude can reach as large as 80% of the incident magnitude, which enhance the focusing efficiency of the NFP, leading to a brighter focus spot. Fig. S4(b) shows the y-polarized electric field intensity distribution at the focal plane I= 1.5 μm originated from the reflective NFP at the wavelength 12 μm. The field profile plotted along the horizontal lines passing the spot center has been depicted in Fig. S4(c). Comparing the calculated results (red solid curve) and the near-field diffraction limit value (green dashed curve), it can be concluded that the reflective metasurface based NFP is also capable of realizing three dimensional subdiffraction focus exceeding the near-field diffraction limit.

Acknowledgements

This work was supported by the National Natural Science Funds (61575032).

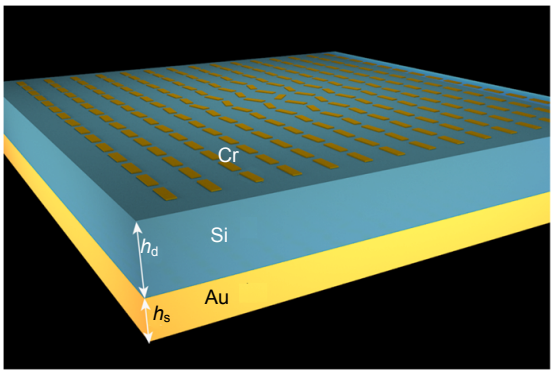

Fig. S3 Schematic of the reflective mode metasurface. The thickness of silicon spacer h_d and the reflective layer h_s are 2.2 μm and 1.5 μm, respectively. All the other structural parameters are the same as the transmitted mode NFP.

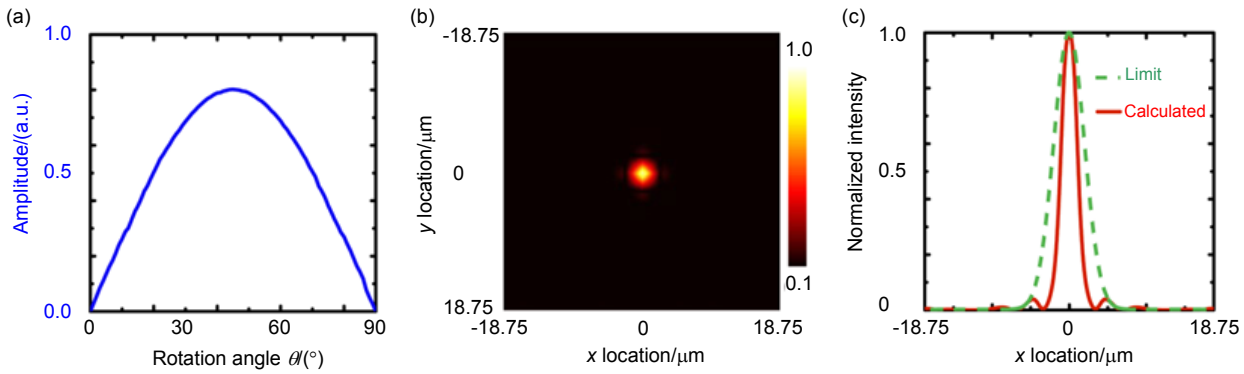

Fig. S4 (a) Calculated cross polarized field amplitude versus the rotation angle of the antenna. The maximum modulated field amplitude reaches 0.8 as normalized to the incident magnitude. (b) Schematic of y-polarized electric field intensity ($|E_y|^2$) distribution at focal plane. (c) The red solid curve indicates the calculated y-polarized field intensity profile, which is narrower than the green dashed curve. It amounts to the focus quality exceeds the near-field diffraction limit as predicted.

References

1 Betzig E, Trautman J K. Near-field optics: microscopy, spectroscopy, and surface modification beyond the diffraction limit[J]. *Science*, 1992, **257**(5067): 189–195.

2 Gramotnev D K, Bozhevolnyi S I. Plasmonics beyond the diffraction limit[J]. *Nature Photonics*, 2010, **4**(2): 83–91.

3 Gramotnev D K, Bozhevolnyi S I. Nanofocusing of electromagnetic radiation[J]. *Nature Photonics*, 2014, **8**(1): 13–22.

4 Shi Haofei, Guo L J. Design of plasmonic near field plate at optical frequency[J]. *Applied Physics Letters*, 2010, **96**(14): 141107.

5 Xu Ting, Agrawal A, Abashin M, *et al*. All-angle negative refraction and active flat lensing of ultraviolet light[J]. *Nature*, 2014, **497**(7450): 470–474.

6 Luo Xiangang, Pu Mingbo, Ma Xiaolinag, *et al*. Taming the electromagnetic boundaries via metasurfaces: from theory and fabrication to functional devices[J]. *International Journal of Antennas and Propagation*, 2015, **2015**: 204127.

7 Pendry J B. Negative refraction makes a perfect lens[J]. *Physical Review Letters*, 2000, **85**(18): 3966–3969.

8 Gordon R. Limits for superfocusing with finite evanescent wave amplification[J]. *Optics Letters*, 2012, **37**(5): 912–914.

9 Fang N, Lee H, Sun Cheng, *et al*. Sub–diffraction-limited optical imaging with a silver superlens[J]. *Science*, 2005, **308**(5721): 534–537.

10 Song Maowen, Wang Changtao, Zhao Zeyu, *et al*. Nanofocusing beyond the near-field diffraction limit via plasmonic Fano resonance[J]. *Nanoscale*, 2016, **8**(3): 1635–1641.

11 Merlin R. Radiationless electromagnetic interference: evanescent-field lenses and perfect focusing[J]. *Science*, 2007, **317**(5840): 927–929.

12 Grbic A, Jiang Lei, Merlin R. Near-field plates: subdiffraction focusing with patterned surfaces[J]. *Science*, 2008, **320**(5875): 511–513.

13 Imani F M, Grbic A. Generating evanescent Bessel beams using near-field plates[J]. *IEEE Transactions on Antennas and Propagation*, 2012, **60**(7): 3155–3164.

14 Grbic A, Merlin R. Near-field focusing plates and their design[J]. *IEEE Transactions on Antennas and Propagation*, 2008, **56**(10): 3159–3165.

15 Lan Lu, Jiang Wei, Ma Yungui. Three dimensional subwavelength focus by a near-field plate lens[J]. *Applied Physics Letters*, 2013, **102**(23): 231119.

16 Cai Wenshan, Shalaev V. Optical Metamaterials[M]. New York: Springer, 2010.

17 Song Maowen, Yu Honglin, Hu Chenggang, *et al*. Conversion of broadband energy to narrowband emission through double-sided metamaterials[J]. *Optics Express*, 2013, **21**(26): 32207–32216.

18 Xu Ting, Wu Y K, Luo Xiangang, *et al*. Plasmonic nanoresonators for high-resolution colour filtering and spectral imaging[J]. *Nature Communications*, 2010, **1**: 59.

19 Pu Mingbo, Hu Chenggang, Huang Cheng, *et al*. Investigation of Fano resonance in planar metamaterial with perturbed periodicity[J]. *Optics Express*, 2013, **21**(1): 992–1001.

20 Boltasseva A, Atwater H A. Low-loss plasmonic metamaterials[J]. *Science*, 2011, **331**(6015): 290–291.

21 Zeng Beibei, Gao Yongkang, Bartoli F J. Ultrathin nanostructured metals for highly transmissive plasmonic subtractive color filters[J]. *Scientific Reports*, 2013, **3**: 2840.

22 Gordon R. Proposal for superfocusing at visible wavelengths using radiationless interference of a plasmonic array[J]. *Physics Review Letters*, 2009, **102**(20): 207402.

23 Chen Shuwen, Jin Shilong, Gordon R. Subdiffraction focusing enabled by a Fano resonance[J]. *Physical Review X*, 2014, **4**(3): 031021.

24 Yu Nanfang, Capasso F. Flat optics with designer metasurfaces[J]. *Nature Materials*, 2014, **13**(2): 139–150.

25 Ni Xingjie, Emani N K, Kildishev A V, *et al*. Broadband light bending with plasmonic nanoantennas[J]. *Science*, 2012, **335**(6067): 427.

26 Kildishev A V, Boltasseva A, Shalaev V M. Planar photonics with metasurfaces[J]. *Science*, 2013, **339**(6125): 1232009.

27 Liu Lixiang, Zhang Xueqian, Kenney M, *et al*. Broadband metasurfaces with simultaneous control of phase and amplitude[J]. *Advanced Materials*, 2014, **26**(29): 5031–5036.

28 Li Xiong, Chen Lianwei, Li Yang, *et al*. Multicolor 3D meta-holography by broadband plasmonic modulation[J]. *Science Advance*, 2016, **2**(11): e1601102.

29 Jin Jinjin, Pu Mingbo, Wang Yanqin, *et al*. Multi-channel vortex beam generation by simultaneous amplitude and phase modulation with two-dimensional metamaterial[J]. *Advanced Materials Technologies*, 2017, **2**(2): 1600201.

30 Cui Jianhua, Huang Cheng, Pan Wenbo, *et al*. Dynamical manipulation of electromagnetic polarization using anisotropic meta-mirror[J]. *Scientific Reports*, 2016, **6**: 30771.

31 Liu Kaipeng, Guo Yinghui, Pu Mingbo, *et al*. Wide field-of-view and broadband terahertz beam steering based on gap plasmon geodesic antennas[J]. *Scientific Reports*, 2017, **7**: 41642.

32 Ma Xiaoliang, Pu Mingbo, Li Xiong, *et al*. Optical phased array radiating optical vortex with manipulated topological charges[J]. *Optics Express*, 2015, **23**(4): 4873–4879.

33 Pu Mingbo, Li Xiong, Ma Xiaoliang, *et al*. Catenary optics for achromatic generation of perfect optical angular momentum[J]. *Science Advances*, 2015, **1**(9): e1500396.

34 Khorasaninejad M, Chen Weiting, Devlin R C, *et al*. Metalenses at visible wavelengths: diffraction-limited focusing and subwavelength resolution imaging[J]. *Science*, 2016, **352**(6290): 1190–1194.

35 Ni Xingjie, Ishii S, Kildishev A V, *et al*. Ultra-thin, planar, Babinet-inverted plasmonic metalenses[J]. *Light*: *Science & Applications*, 2013, **2**(4): e27.

36 Chen Xianzhong, Huang Lingling, Mühlenbernd H, *et al*. Dual-polarity plasmonic metalens for visible light[J]. *Nature Communications*, 2012, **3**: 1198.

37 Huang Lingling, Chen Xianzhong, Mühlenbernd H, *et al*. Dispersionless phase discontinuities for controlling light propagation[J]. *Nano Letters*, 2012, **12**(11): 5750–5755.

38 Tang Dongliang, Wang Changtao, Zhao Zeyu, *et al*. Ultrabroadband superoscillatory lens composed by plasmonic metasurfaces for subdiffraction light focusing[J]. *Laser & Photonics Review*, 2015, **9**(6): 713–719.

39 Palik E D. Handbook of Optical Constants of Solids[M]. New York: Academic, 1985.

40 Pors A, Nielsen M G, Eriksen R L, *et al*. Broadband focusing flat mirrors based on plasmonic gradient metasurfaces[J]. *Nano Letters*, 2013, **13**(2): 829–834.

41 Alonso-Gonzalez P, Schnell M, Sarriugarte P, *et al*. Real-space mapping of fano interference in plasmonic metamolecules[J]. *Nano Letters*, 2011, **11**(9): 3922–3926.